

# Programmable Aerodynamic Drag on Active Dimpled Cylinders

Mark Guttag, Dong Yan, and Pedro M. Reis\*

This study demonstrates that the aerodynamic drag profile of a patterned deformable cylinder at high Reynolds numbers can be programmed, on demand, by modifying its topography through pneumatic actuation. The samples used in the experiments comprise a rigid tube containing a hexagonal array of holes, over which an elastomeric cylindrical membrane is stretched. Decreasing the internal pressure of the structure causes an inward deflection of the outer membrane over the holes, thereby producing a regular pattern of dimples. The depth of these dimples can be controlled by tuning the pressure differential. The relationship between the mechanical deformation of the membrane and the pneumatic loading is characterized using a combination of finite element simulations and precision mechanical experiments. Wind tunnel experiments are performed to study how both the depth and the diameter of the dimples dictate the aerodynamic performance of the samples in the critical Reynolds number regime. Finally, the tunable nature of the specimens is exploited to automatically control the dependence of the drag coefficient on the Reynolds number, toward targeting predefined drag profiles.

## 1. Introduction

Golf balls are a canonical example of the usage of dimpled surfaces for aerodynamic drag reduction. From the inception of the game of golf, there has been a desire to maximize the length that a ball will travel. In 1845, with the introduction of a soft remoldable ball known as the ‘Gutta-percha,’ it was recognized that balls with marked up surface defects due to continued use flew farther than smooth, pristine balls.<sup>[1]</sup> The first patent for a golf ball with a dimpled topography was based on this observation.<sup>[2]</sup> Subsequently, there has been a significant

number of studies on employing dimples and other patterned surfaces to reduce drag or control flow.<sup>[1,3–12]</sup>

Smooth bluff bodies, such as cylinders and spheres, under high Reynolds number flow conditions, undergo a phenomenon known as the drag crisis.<sup>[13]</sup> Hereon, we refer to the Reynolds number as  $Re = UD/\nu$ , where  $\nu$  is the kinematic viscosity of the fluid,  $U$  is the characteristic velocity of the flow, and  $D$  is the characteristic length scale of the object (e.g., diameter). The drag crises for high values of the  $Re$  (typically  $>10^4$ ) is comprised of four regimes depending on the value of  $Re$ . 1) In the *sub-critical regime*, the drag coefficient,  $C_d$  remains nearly constant with increasing  $Re$ .<sup>[14–16]</sup> Above a threshold Reynolds number ( $Re \approx 2 \times 10^5$  for smooth cylinders),  $C_d$  drops sharply in what is known as the 2) *critical regime*.<sup>[15,16]</sup> After reaching a minimum,  $C_d$  then increases with increasing  $Re$  in the 3) *supercritical regime*, and, finally, a plateau is reached in

the 4) *transcritical regime*.<sup>[15,16]</sup> Several studies have investigated the drag on bluff bodies in the neighborhood of this drag crisis.<sup>[1,3,5,6,15–18]</sup> In a seminal study, Achenbach<sup>[15,16]</sup> performed wind tunnel experiments on both smooth and uniformly roughened spheres and observed that as the  $Re$  was increased, past a drag coefficient minimum, a steep increase and subsequent plateau of  $C_d$  were observed in the supercritical and transcritical regimes, respectively. Subsequently, Bearman and Harvey<sup>[1]</sup> tested golf balls in a wind tunnel and found that the dimples anticipated the drag crisis when compared to the rough spheres<sup>[15,16]</sup>; after the initial drop in  $C_d$ , the steep increase in  $C_d$  generally associated with the supercritical regime did not occur.<sup>[1]</sup> Instead,  $C_d$  only increased slightly with  $Re$  past the critical regime.

More recently, the mechanism for drag reduction and subsequent nearly constant drag coefficient of dimpled spheres has been investigated by Choi et al.,<sup>[5]</sup> finding that the flow separates at the front edge of the dimples, and reattaches at their back-edge. The separation bubble that ensues is similar to that observed in the critical regime on a smooth sphere.<sup>[3,5]</sup> After the flow reattaches, the increased momentum in the boundary layer generated by the separation bubble delays the final separation point.<sup>[5]</sup> The continuing presence of the separation bubbles over the dimples, even after the initial drop in  $C_d$ , is different from the case of rough spheres, for which, after the critical Reynolds number, the boundary layer directly transitions to turbulence

Prof. P.M. Reis, Dr. M. Guttag, Dr. D. Yan  
Flexible Structures Laboratory  
Institute of Mechanical Engineering  
Ecole Polytechnique Fédérale de Lausanne  
Station 9, 1015 Lausanne, Switzerland  
E-mail: pedro.reis@epfl.ch

Dr. M. Guttag  
Department of Mechanical Engineering  
Massachusetts Institute of Technology  
77 Massachusetts Avenue, 02139 Cambridge, MA, USA

 The ORCID identification number(s) for the author(s) of this article can be found under <https://doi.org/10.1002/adem.201801315>.

DOI: 10.1002/adem.201801315

and the drag coefficient increases significantly.<sup>[19]</sup> In the subcritical regime, the increase in momentum caused by the separation bubbles in the earlier dimples is not high enough to overcome the adverse pressure gradient and delay the main separation. Thus the  $C_d$  is still high (for spheres  $C_d = 0.5$ ).<sup>[5]</sup> Aoki et al.<sup>[17]</sup> later discovered that deeper dimples cause the separation bubble to occur further upstream (closer to the front of the body), explaining the lower critical Reynolds number and the higher minimum  $C_d$  observed for the specimens with deeper dimples.<sup>[17]</sup>

Terwagne et al.<sup>[18]</sup> systematically examined the effect of the dimple depth on aerodynamic drag by making use of a wrinkling instability of a thin-stiff shell bound to a thick-soft substrate to generate a dimpled pattern with tunable depth on spherical specimens. Dimples formed and their amplitude could be varied by depressurizing a spherical cavity inside the samples to induce increasing levels of compression. Wind tunnel tests yielded results consistent with previous studies: increasing the dimple depth induced an earlier drag crisis and a higher minimum drag coefficient.<sup>[17,18]</sup> Therefore, at high  $Re$  a shallower dimpled specimen may have a lower  $C_d$  than a deeper dimpled one. However, at a lower  $Re$ , the opposite may be true. As a result of this behavior, there is no universal optimal dimple depth across a wide range of  $Re$ . Furthermore, this active system demonstrated the possibility for the topography of a bluff body to be changed on-demand, thereby opening the door for flow control. As such, the dimple depth could be actively varied with a single input signal (the pressure differential across the sample) toward minimizing  $C_d$  depending on the flow conditions (for a given value of  $Re$ ).<sup>[18]</sup>

Even if spheres are the most commonly tested geometry with dimples given the direct analogy with golf balls, other geometries such as cylinders have also been studied.<sup>[6,20,21]</sup> Similarly to the spherical counterpart discussed above, the drag crisis for dimpled cylinders has been shown to occur earlier than for a smooth cylinder.<sup>[6]</sup> Moreover, above the critical Reynolds number, the drag coefficient for a cylinder with dimples does not increase as much as for a sand-roughened cylinder with a similarly scaled roughness.<sup>[6]</sup>

In our previous work, we performed wind tunnel experiments on cylinders with axial grooves, whose depths could be pneumatically controlled.<sup>[22]</sup> Through careful study of the effect of the groove depth on the drag coefficient, we were able to use the tunable nature of the groove depth to minimize the drag coefficient over a range of Reynolds numbers around the critical regime.<sup>[22]</sup> In addition to modifying the shape of the surface, other active methods for controlling the drag have been studied. One heavily studied active drag reduction strategy is the use of oscillatory motion.<sup>[23–27]</sup> The oscillation of cylinders is intended to alter the structure and frequency of the vortex shedding in their wake. Another active method for reducing drag utilizes time-periodic fluid injection and suction at the surface of bodies to directly affect the boundary layer.<sup>[3,28,29]</sup>

Here, we systematically study the effect of the geometry and topography of a pattern of deformable dimples on the aerodynamic performance of cylindrical specimens that can be dynamically actuated pneumatically, on-demand. Our samples enable us to span a wide range of dimple depths with a single specimen. Wind tunnel tests are performed to

characterize the dependence of the aerodynamic drag of our morphable cylinders on the primary parameters. With these data at hand, we then demonstrate the possibility to tune and program different drag profiles (on the same sample) as a function of Reynolds number, in ways that are not possible in static systems. Our proposed mechanism for drag control should easily be adapted and utilized in a variety of settings where bluff bodies are exposed to variable flow conditions.

## 2. Fabrication of Samples and Experimental Setup

Our morphable cylindrical structure comprised a rigid acrylic tube with an array of laser-cut through holes on its surface, which acts as a skeleton. A thin cylindrical shell was then made from a flexible latex membrane and stretched over the acrylic skeleton. This design was inspired by our previous work on grooved cylinders,<sup>[22]</sup> but this time with a dimpled geometry. By depressurizing the inside of the cylinder, the latex membrane deflected inward, into the holes, thereby forming dimples. These dimples were circular depressions on the surface, with a diameter fixed by the size of the laser-cut holes in the base acrylic cylinder. The depth of the dimples was varied by changing the magnitude of the applied pressure differential.

### 2.1. Sample Fabrication

In **Figure 1a** and **b**, we show schematic diagrams of the layout of the dimpled specimens; top view and a cross-sectional view, respectively. The specimens were made of a rigid acrylic tube with an outer diameter of  $D = 50.8$  mm and a wall thickness of 3.175 mm. Using a rotary fixture of the laser cutter (Laser Pro, Spirit GLS), circular holes were cut into the cylinder, and the tube was cut to a length of 44.5 cm. These holes were arranged on the surface of the cylinders in a uniform hexagonal lattice with horizontal rows aligned along the  $x$ -axis, as shown in **Figure 1a**. The rows of holes are equally spaced, such that there are 12 rows around the circumference of the specimens. Therefore, the spacing between rows along the surface was  $\pi D/12 \approx 13.3$  mm. The axial spacing between holes was the same as the spacing between rows, and every other row was set out of phase to create the hexagonal array shown in **Figure 1a**. The following values for the dimple diameters were explored:  $w = \{4.64, 5.82, 6.98, 8.14, 9.30, 10.70\}$  mm.

Once the acrylic base tubes were prepared, the latex membranes were manufactured. Thin latex sheets (thickness  $t = 0.25$  mm and shear modulus  $G = 464 \pm 15$  kPa) were cut into rectangles. The ends of the rectangles were glued together using rubber cement (Best Test) to form tubes with a diameter of 36.9 mm. These latex tubes were then stretched over the acrylic cylinders, and the ends were sealed with O-rings, as shown in **Figure 1a**. The radial pre-stretch in the film was measured to be  $\lambda_{\text{rad}} = 1.38 \pm 0.01$ . This pre-stretch was important to ensure that no fluttering of the latex membrane occurred when the specimens were placed into the wind tunnel. Both ends of the acrylic base cylinder were capped, and one end was connected to a vacuum pump (DOA-P704-AA, Gast). An electronic pressure

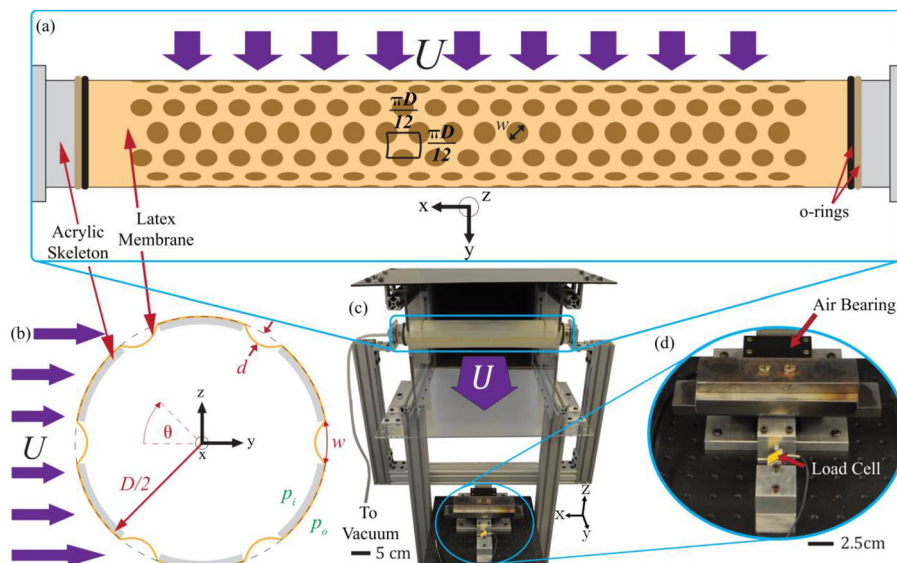


**Figure 1.** Experimental setup. a) Schematic diagram (top view) of the cylindrical specimens tested in the wind tunnel. b) Schematic diagram (cross section) of the specimens. c) Photograph of the experimental apparatus. The specimen spans the full width of the wind tunnel. d) Close up view of the load cell (connected to the air bearing) used to measure the aerodynamic drag force.

control valve (QPV1, Proportion-Air, Inc.) maintained a pressure differential,  $\Delta p = p_o - p_i$ , across the membrane.

## 2.2. Experimental Apparatus

For the wind tunnel experiments, we employed the same experimental apparatus that we used in our previous investigation on grooved cylinders.<sup>[22]</sup> The samples were placed across the test section of an open exhaust wind tunnel with a cross-section of  $30.5 \times 30.5 \text{ cm}^2$ , as shown in Figure 1c. The wind tunnel was capable of producing steady flow speeds  $5 < U [\text{ms}^{-1}] < 45$  with a turbulence intensity, defined as fluctuations from the mean velocity, of less than 1%. The wind speed was recorded by a high-accuracy capacitance manometer (690A Baratron). Throughout, we define the Reynolds number as

$$Re = \frac{UD}{\nu}, \quad (1)$$

where  $\nu$  is the kinematic viscosity of air and the diameter of the specimen,  $D$  is taken as the characteristic length.

The specimen was secured at its two end caps to a U-shaped aluminum frame which was fastened to one end of a linear air bearing (RAB2, Nelson Air Corp.). The other end of the air bearing was connected to a load-cell (LRM200 Miniature S-Beam Load Cell, Futek) as shown in Figure 1d. The forces on the sample in the  $y$ -direction (i.e., the drag forces) were measured directly by the load-cell, whose signal was digitized with a data-acquisition system (DAQ, USB-6008, National Instruments). With this setup, we were able to simultaneously measure and record the wind speed and drag forces while also controlling the pressure inside the sample,  $p_i$ , and thus the depth of the dimples.

## 3. Mechanics of Deformation of the Dimpled Surface

Applying a pressure differential across the samples caused the latex membrane to stretch inward, causing the dimples to deepen. In this section, we present the results of mechanical experiments and simulations using the finite element method (FEM) designed to predictively describe how the shape of the dimples, specifically their depth,  $d$ , is set by the applied pressure differential,  $\Delta p$ . This  $d(\Delta p)$  dependence, shall be used in Section 4 for the wind tunnel experiments.

### 3.1. Measurement of the Dimple Depth

To characterize the mechanical deformation in the film, we performed a series of experiments where the pressure differential across the membrane was set to a value in the range  $0 < \Delta p [\text{kPa}] < 24$ , and the topography of the specimens was then quantified using a 3D laser scanner (3D Scanner Ultra HD, NextEngine). This 3D scanner was placed above and oriented parallel to the specimen, as shown in Figure 2a. The 3D-scans captured approximately one-third of the circumference of the cylindrical specimens, which was sufficient to determine the average dimple depth that was otherwise uniform across the sample. The 3D-scans produced a point cloud with  $(x, y, z)$  coordinates of the surface topography. Figure 2b–d shows photographs and the corresponding 3D point clouds of a representative sample with dimple diameter  $w = 9.30 \text{ mm}$  and applied pressures of  $\Delta p = 0, 10, \text{ and } 20 \text{ kPa}$ .

The dimple depth is defined relative to a smooth cylinder (i.e., a perfect cylinder would have a dimple depth of 0), as shown in the schematic diagram of Figure 1b. A custom Matlab code was used to extract the depth of each dimple from the 3D point cloud

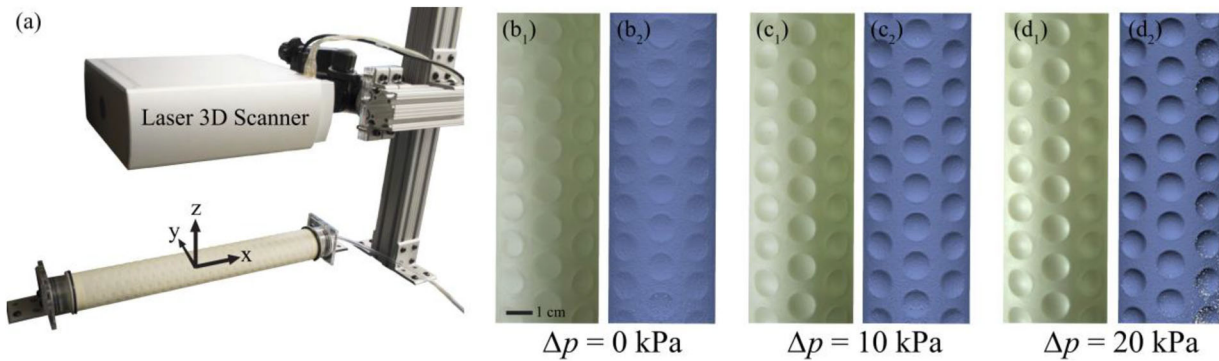


**Figure 2.** Experimental setup used to measure the depth of the dimples. a) Photograph of the laser 3D scanner mounted above the dimpled cylindrical specimens. b–d) Photographs and the corresponding 3D scanned profiles of a dimpled specimen with  $w = 9.30$  mm and applied pressures of  $\Delta p = 0, 10,$  and  $20$  kPa, respectively.

data. The mean depth of all the dimples on a specimen,  $d$ , was taken as the characteristic dimple depth for that specimen.

### 3.2. Dependence of the Dimple Deformation on the Pneumatic Actuation

The dependence of the dimple depth,  $d$ , on the pressure differential,  $\Delta p$ , is shown in **Figure 3a**, for specimens with dimple diameters of  $w = \{4.64, 5.82, 6.98, 8.14, 9.30, 10.70\}$  mm. In this plot, the error bars on the data points correspond to the standard deviation of between 3 and 8 experiments with different specimens. In the base state, with  $\Delta p = 0$  kPa, there is a non-zero dimple depth for all of the specimens, as we explain next. Recall that the dimple depth is defined relative to the smooth cylinder, as shown in **Figure 1b**. When the latex membrane is initially stretched over the body of the cylinder, the latex will cover the holes such that there is no curvature in the film. This means that a section of the circular cross-section has been cut off by the membrane, and so, even before any vacuum pressure is applied, the specimens are not smooth cylinders. Since the dimple diameter acts as a chord length when  $w/D$  is increased the sagitta grows. Based on our definition of  $d$ , the sagitta is equal to the initial dimple depth,  $d_0$ . Therefore, as  $w/D$  increases, so does  $d_0$ . The y-axis on the right side of the plot in **Figure 3a** shows the normalized dimple depth,  $d^* = d/D$ . In Section 4, we will use this

normalized dimple depth when examining the aerodynamics of our samples.

In parallel to the physical experiments, we performed finite element modeling (FEM) considering both geometric and material nonlinearities using Abaqus/Standard 6.14. Given the periodicity of the system, the model was simplified to one periodic unit cell with the dimensions of  $\pi D/6$  in the circumferential direction,  $\pi D/12$  in the axial direction, and thickness  $t$ . Further, due to symmetry, we considered one-fourth of the periodic unit cell with symmetric or periodic boundary conditions on the corresponding edges in FEM. The acrylic base tube was simulated with rigid elements (R3D4), while the latex membrane was simulated with solid hybrid elements (C3D8H). A convergence study led to the selection of a non-uniform mesh with 18,400 elements for the acrylic base tube, which was finer near the edges of the holes and coarser in between holes, and of a regular mesh for the latex membrane with 150 elements along the circumferential direction, 75 elements along the axial direction, and 6 elements through the thickness.

A neo-Hookean hyperelastic constitutive model was used for the elements in the latex membrane, with the shear modulus of  $G = 464 \pm 15$  kPa obtained from experiments. A hard and frictionless contact was assigned between the acrylic base tube and the latex membrane. Suitable artificial damping was applied in the simulations to achieve cost-effective solutions without

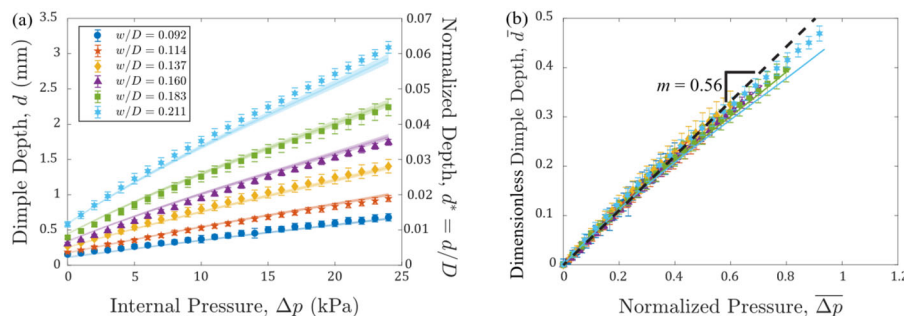


**Figure 3.** a) Experimental and FEM results showing the dependence of the dimple depth on the internal pressure for specimens, for several dimple diameters (see legend). b) Dimensionless dimple depth ( $d^* = [d - d_0]/[w/2]$ ) versus normalized pressure ( $\Delta \bar{p} = [\Delta p w/2]/[\sigma_0 t]$ ) for specimens with several different dimple diameters.

distortions. We performed the simulations using the same protocol as that of the experiments: first pre-stretching the cylindrical latex membrane over the acrylic base tube and then depressurizing the latex membrane by applying uniform negative pressure to its inner surface. This pneumatic loading was implemented as a live pressure, ranging from 0 to 24 kPa.

The FEM results are plotted as solid lines in Figure 3a and the shaded region around the FEM data represent the propagation of errors due to the experimentally measured uncertainty in the shear modulus of the latex membrane. Excellent agreement is found between the experiments and the FEM simulations.

To further study the mechanics of deformation of the dimples, we define a shifted dimple depth,  $d' = d - d_0$ , which in the base state of  $\Delta p = 0$ , yields  $d' = 0$ . Aiming for a more general description of the data for specimens with different dimple diameters, which can subsequently act as a set of design guidelines for the wind tunnel experiments, we turned to a similar problem found in the literature. A study by Cao et al.<sup>[30]</sup> examined the delamination of a graphene film on a substrate. The delamination occurred at the edge of a circular blister that was being inflated.<sup>[30]</sup> Assuming the blisters were axisymmetric, Cao et al. solved the governing differential equation for the deflection of a membrane to determine the shape of the blisters upon inflation.<sup>[30]</sup> This process yielded an analytical solution for the height of an inflated blister.

While our scenario is not identical to that of Cao et al. (in our case no delamination takes place given that  $p_i < p_o$  and the film deforms into the hole), we use their analytical solution as guidance for determining an appropriate scaling of the dimple depth versus pressure. According to this analytical solution of Cao et al.,<sup>[30]</sup> in the limit of large interfacial toughness, the depth of our dimples should scale as:

$$\frac{d'}{w} \propto \frac{\Delta p w}{\sigma_0 t}, \quad (2)$$

where  $t$  is the thickness of the film, and  $\sigma_0$  is its pre-stress. From now on, we shall refer to  $\bar{d} = d'/(w/2)$  as the dimensionless dimple depth, and to  $\bar{\Delta p} = \Delta p(w/2)/(\sigma_0 t)$  as the dimensionless applied pressure. In Figure 3b, the above scaling is used to replot the raw data of Figure 3a, finding that the dimensionless dimple depth and pressure data collapse onto a single line. However, note that the slope of the collapsed data is approximately 0.56, which is different from the analytical pre-factor of 0.25 predicted by Cao et al.<sup>[30]</sup> The difference between our results and the analytical solution could be attributed to various factors. For example, we use the unstressed thickness of the membrane,  $t_0$ , to nondimensionalize the pressure. However, if we assume the latex is incompressible ( $\lambda_{\text{cir}}\lambda_{\text{axi}}\lambda_t = 1$ ), then, using the values for  $\lambda_{\text{rad}}$  and  $\lambda_{\text{cir}}$  measured in experiments, we can calculate the pre-stretch through the thickness to be  $\lambda_t = 0.84$ . From this value of pre-stretch, we find that the thickness of the latex at  $\Delta p = 0$  kPa is  $t^0 = 0.213$  mm. Using  $t^0$  instead of  $t_0$ , we find a slope of approximately 0.45 for the slope of the curve in Figure 3b, which is closer to that of the analytical solution (0.25). While the exact pre-factor of the analytical solution is not recovered for our experiments, the scaling presented in Equation (2) does lead to an excellent collapse of the data, and this is all that was

required to proceed to the wind tunnel experiments taking the results in Figure 3b, along with Equation (2) as a set of design guidelines.

## 4. Wind Tunnel Experiments

We proceed with wind tunnel experiments to characterize the aerodynamic performance of our morphable dimpled cylinders. In particular, we quantify how varying the depth and diameter of their dimples can affect the dependence of the drag coefficient,  $C_d$ , versus the Reynolds number of the flow, within the experimentally available range from  $\text{Re}_{\text{min}} = 3 \times 10^4$  to  $\text{Re}_{\text{max}} = 14.5 \times 10^4$ .

We performed both *fixed* and *active* dimple experiments. In the *fixed* experiments, we measured the  $C_d$  across the full range of Re, while setting  $\Delta p$  to a fixed value, and thus a constant dimple depth. It is important to note that the maximum pressure due to the flow (i.e., the stagnation pressure) was only approximately 1.1 kPa (and this value was only reached at the highest Re). As such, the magnitude of the vacuum pressure being directly applied was large compared to the pressure differences on the surface arising from the fluid motion and any deformation in the film due to the flow can be neglected. In the *active* experiments, we varied  $\Delta p$  as Re changed to achieve a desired dependence of  $C_d$  on Re. The fixed dimple experiments were performed first to explore the effect of different geometric parameters on the aerodynamic performance. We then used the results of the fixed experiments to achieve a desired drag profile in the active dimple experiments.

### 4.1. Experimental Protocol

In the fixed dimple experiments, the dimple diameter was set by the specimen selected. The dimple depth for each specimen, on the other hand, could be gradually and systematically varied through pneumatic actuation. Each experiment was performed by fixing the internal pressure in the specimen, and thus the dimple depth, as discussed in Section 3. For all the specimens, the values of the pressure tested were in the range  $0 < \Delta p$  [kPa]  $< 24$ , which yielded dimple depths in the range of  $0.157 < \bar{d}$  [mm]  $< 3.09$ , depending on the diameter of the dimples, as shown in Figure 3a. In Section 3.2 we defined a dimensionless dimple depth,  $\bar{d}$ . However, the following definition is more commonly used in the literature<sup>[1,5,6,17]</sup>:  $\bar{d}^* = \bar{d}/D$ . From the results in Section 3.2, we can readily convert from  $\bar{d}$  to  $\bar{d}^*$ , and for the remainder of this section we will refer to  $\bar{d}^*$  as the normalized dimple depth, which will vary in the range  $0.3 \times 10^{-2} < \bar{d}^* < 4.5 \times 10^{-2}$ .

During testing, the wind speed was slowly increasing at a rate of  $\dot{U} = 0.05 \text{ m s}^{-2}$ , up to a maximum speed of  $U = 43 \text{ m s}^{-1}$ . As in our previous work on grooved cylinders,<sup>[22]</sup> blockage effects needed to be considered. For this, we used Maskell's theory<sup>[31]</sup> to correct the drag measurements according to

$$C_d = \frac{\bar{C}_d}{1 + \epsilon \beta \bar{C}_d}, \quad (3)$$

where  $\overline{C_d} = \frac{2F_d}{\rho U^2 LD}$  is the uncorrected drag coefficient (measured raw),  $\beta = DL/L^2 = 0.167$  is the blockage ratio, and  $\epsilon = 0.3453$  is a fitting parameter that was determined following the same experimental protocol used in our previous work.<sup>[22]</sup> With this correction, each fixed experiment yielded the drag coefficient as a function of Reynolds number,  $C_d(Re)$ , for a single dimple depth.

#### 4.2. Characterizing Drag Coefficients versus dimple geometry

We proceed by studying the effect on the aerodynamic performance of two geometric parameters of the individual dimples: the normalized dimple depth,  $d^* = d/D$ , and the normalized dimple diameter,  $w/D$ . For the latter, we considered specimens with 6 different values:  $w/D = \{0.091, 0.155, 0.137, 0.160, 0.183, 0.211\}$ .

Each panel in **Figure 4** shows experimental results of the drag coefficient as a function of Reynolds number for a single specimen (i.e., a single value of  $w/D$ ), over a range of normalized dimple depths. The various symbols represent different values of the dimple size and will remain consistent in subsequent plots. Each curve represents the average of three identical experiments. For each specimen, the dimple depth was changed by varying the pressure over the range,  $0 \leq \Delta p$  [kPa]  $\leq 24$ . The color bar on the right side of **Figure 4** represents the normalized dimple depth: blue and red correspond to shallower and deeper dimples, respectively. Even though the range of  $\Delta p$  was the same across specimens, the difference in dimple diameter led to a variation in the range of depth for each specimen. Since the diameter of the cylinder,  $D$ , is constant,

this leads to a different range of  $d^*$  for each specimen. For example, **Figure 4a** shows the results of experiments on a specimen with  $w/D = 0.091$ , which could achieve normalized dimple depths of  $d^* = 0.3 \times 10^{-2}$  to  $1.4 \times 10^{-2}$ . The results shown in **Figure 4f** are for the specimen with the largest dimples,  $w/D = 0.211$ , which could reach normalized dimple depths of  $d^* = 1.2 \times 10^{-2}$  to  $4.45 \times 10^{-2}$ . This variation in the range of  $d^*$ , is captured visually by the different span of colors shown in each panel.

Focusing first on the results for the sample with  $w/D = 0.091$  (the smallest dimple diameter tested), **Figure 4a**, we observe that for the shallowest dimples,  $d^* = 3 \times 10^{-3}$  (dark blue), there is no sharp drop in drag coefficient; that is, the drag crisis does not take place in the explored range of  $Re$ . For the deepest dimples,  $d^* = 1.4 \times 10^{-2}$ , the drag crisis begins at  $Re \approx 5.4 \times 10^4$ , and the critical Reynolds number (where the drag is a minimum) is  $Re^* = \{1.17 \pm 0.03\} \times 10^5$ . Most of the dimple depths tested for this specimen exhibit a decreasing  $C_d(Re)$  up to the maximum experimental Reynolds number tested,  $Re_{max}$ , indicating that, for those dimple depths, the specimen is still in the critical regime, thus  $Re^* > Re_{max}$ . Even for the few depths large enough to observe the minimum drag coefficient,  $Re^*$  is close to  $Re_{max}$ , so we do not observe the behavior in the supercritical and transcritical regimes.

The results of experiments on specimens with dimples sizes  $w/D = 0.115$  and  $0.137$  are shown in **Figure 4b** and **c**, respectively. In these experiments, the shallowest dimples show the initiation of the drag crisis near  $Re_{max}$  ( $Re \approx 1.2 \times 10^5$  and  $Re \approx 1.1 \times 10^5$  for  $w/D = 0.115$  and  $w/D = 0.137$ , respectively). For both of these specimens, even when the maximum pressure differential was applied ( $\Delta p = 24$  kPa) and the deepest dimples were attained, the initiation of the drag crisis (and a portion of the subcritical regime) can be observed in the experimental range of Reynolds number.

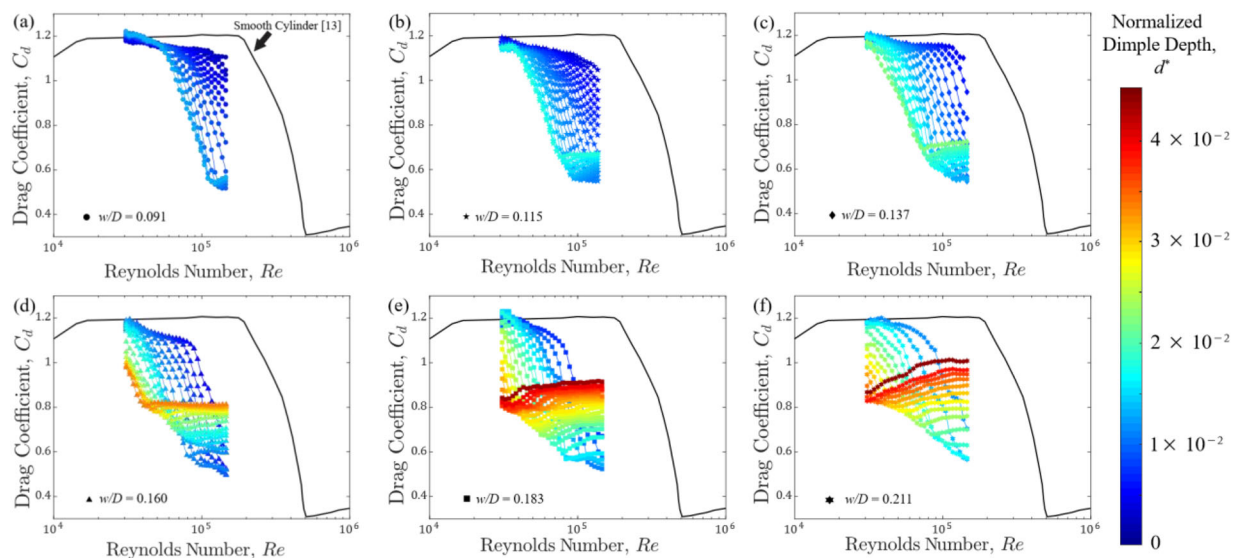


**Figure 4.** Dependence of drag coefficient,  $C_d$ , on Reynolds number,  $Re$ , for different values of the dimple depth and dimple diameter. The colors represent the normalized dimple depth,  $d^* = d/D$ , as given by the adjacent color bar. Each plot corresponds to a value of  $w/D$ : a–f) for samples with  $w/D = \{0.091, 0.115, 0.137, 0.160, 0.183, 0.211\}$ , respectively. The black lines are the results of experiments by Wieselsberger<sup>[13]</sup> on a smooth cylinder.

For the specimens with  $w/D \geq 0.160$ , the shallowest dimples yield results where large portions of the critical regime are observed. The results for the deepest dimples tested for each of these specimens show none of the features associated with the subcritical regime, even at the lower limit of experimental Reynolds number,  $Re_{\min}$ . The deepest and largest dimples, shown in Figure 4f ( $w/D = 0.211$  and  $d^* = 4.45 \times 10^{-2}$ ), exhibit a monotonically increasing drag coefficient in the experimental range, which indicates that the critical Reynolds number is below  $Re_{\min}$  ( $Re^* < 3 \times 10^4$ ).

Looking at all of the data in Figure 4, it is clear that each specimen spans a different portion of the  $(C_d, Re)$  space. The smaller dimples can maintain a higher  $C_d$  at high  $Re$ , while the larger dimples can reach lower  $C_d$  at low  $Re$ . For each specimen, we observe that, as the dimple depth is increased, the drag crisis occurs earlier and the minimum value of  $C_d$  increases. This is consistent with the results for previous studies on dimples<sup>[17,18]</sup> and our previous work on grooved cylinders.<sup>[22]</sup> Each of the panels in Figure 4 represents a specimen with a different dimple diameter, tested at various depths. Note that certain colors (and thus dimple depths) span similar portions of the  $(C_d, Re)$  space. This similarity between plots was the first indication that, across specimens and therefore across different dimple diameters, a given depth may yield similar drag profiles. The effect of the dimple depth on  $C_d(Re)$  can be more easily explored by grouping curves with similar  $d^*$  for different specimens.

Figure 5 shows the dependence of the drag coefficient on the Reynolds number, for different normalized dimple depths. The data plotted here is the same as that shown in Figure 4, and represents experiments on specimens with six different sized dimples ( $w/D = 0.091$  to  $0.211$ ). Each panel was plotted by selecting a normalized dimple depth ( $d^* = \{0.5, 1.0, 1.6, 2.0, 2.4, 3.0, 3.4, 3.9\} \times 10^{-2}$ , for Figure 5a–h, respectively) and finding experiments that were performed with a  $d^*$  within 5% of that value. The different symbols represent the different dimple diameters, and thus different specimens.

Focusing on Figure 5a, note that the two curves correspond to data obtained from experiments on specimens with  $w/D = 0.091$  and  $0.115$ . The specimens with larger dimples are not represented in this plot since, even when  $\Delta p = 0$ ,  $d^* > 0.5 \times 10^{-2}$ . This is because larger dimples cut off a larger portion of the circular cross section of the cylinder, thus leading to a higher initial dimple depth,  $d_0$ , as discussed in Section 3.2. Not all specimens span the same range of  $d^*$ , and thus the different panels in Figure 5 are populated with experimental results of different specimens.

Increasing the dimple depth to  $d^* = 1.0 \times 10^{-2}$ , Figure 5b shows results from more specimens (all dimple diameters tested except  $w/D = 0.211$ ). For the deepest dimples,  $d^* = 3.9 \times 10^{-2}$  shown in Figure 5h, we only see results for the two specimens with the largest dimple diameter ( $w/D = 0.183$  and  $0.211$ ). In each panel, different specimens with the same normalized dimple depth exhibit similar results. Therefore, for a given normalized dimple depth,  $C_d(Re)$  is independent of the dimple diameter,  $w/D$ . Additionally, from the differences between panels, we observe that changing the normalized dimple depth, causes the  $C_d(Re)$  relationship to vary. From these observations, we can conclude that the aerodynamic drag

performance is controlled by the depth of the dimples, and is independent of the dimple diameter.

### 4.3. Programming of the Drag Coefficient Profile

In our previous work on grooved cylinders,<sup>[22]</sup> we demonstrated the ability to actively change the surface shape to minimize the drag coefficient under changing flow conditions. In this section, we follow a similar procedure in which we use the information learned from the fixed experiments performed in Section 4.2 to program the drag coefficient in predetermined ways. The procedure uses the fixed specimen data to determine the dimple depth, and therefore the value of  $\Delta p$ , necessary to achieve a desired drag coefficient at a given Reynolds number. This required  $\Delta p$  is then applied to the sample using the digital pressure regulator. As the wind speed changes, the system automatically updates the pressure being applied to the sample and the drag force is measured. With this method, we are able to actively minimize the drag coefficient with results similar to those in our previous work on grooved cylinders.<sup>[22]</sup>

Having successfully created a system that could adapt the shape of the surfaces to minimize the drag coefficient, we now explore the possibility of using the active system to program other functional dependencies of the drag coefficient on the Reynolds number,  $C_d(Re)$ . Specifically, we attempted to attain the following  $C_d(Re)$  profiles: 1) constant, 2) increasing, and 3) decreasing. To do so, we utilize the active control loop system, described above, on a specimen with  $w/D = 0.115$ . This particular specimen was chosen because of the relative ease of precisely controlling the dimple depth.

We first discuss the case in which we target to maintain  $C_d = 1.0$  for the range  $5.24 < Re [\times 10^4] < 13.7$ , as shown by the solid magenta line in Figure 6b. For a given  $Re$ , we determined which static dimple depths gave the closest  $C_d$  both above and below  $C_d = 1.0$ .

We define the static dimple depth that produced the closest  $C_d^+ = C_d > 1.0$  as  $d^{*+}$ , and the depth that yielded the closest  $C_d^- = C_d < 1.0$  as  $d^{*-}$ . We linearly interpolated between these two static experiments to determine the  $d^*$  (and thus  $\Delta p$ ) value required to achieve  $C_d = 1.0$  at a given  $Re$ :

$$d^* = \frac{(1.0 - C_d^+)(d^{*-} - d^{*+})}{C_d^+ - C_d^-} + d^{*+}. \quad (4)$$

The interpolated  $d^*$  values are shown with the magenta stars in Figure 6a. In order to use the control loop described above, we needed to fit a continuous function to the interpolated data. In this work, the quality of the continuous functional fit to the data is only important in our experimental range of Reynolds number. We do not aim to make a prediction outside of this range, and therefore, any functional form that fits the interpolated data well can be used. After trying multiple functions, we determined that a fifth order polynomial fit the data reasonably well, as shown by the solid magenta line in Figure 6a. The results of the active experiments are shown in Figure 6b with the star symbols.

With the same specimen ( $w/D = 0.115$ ), we also demonstrated the ability to maintain other constant drag coefficients,

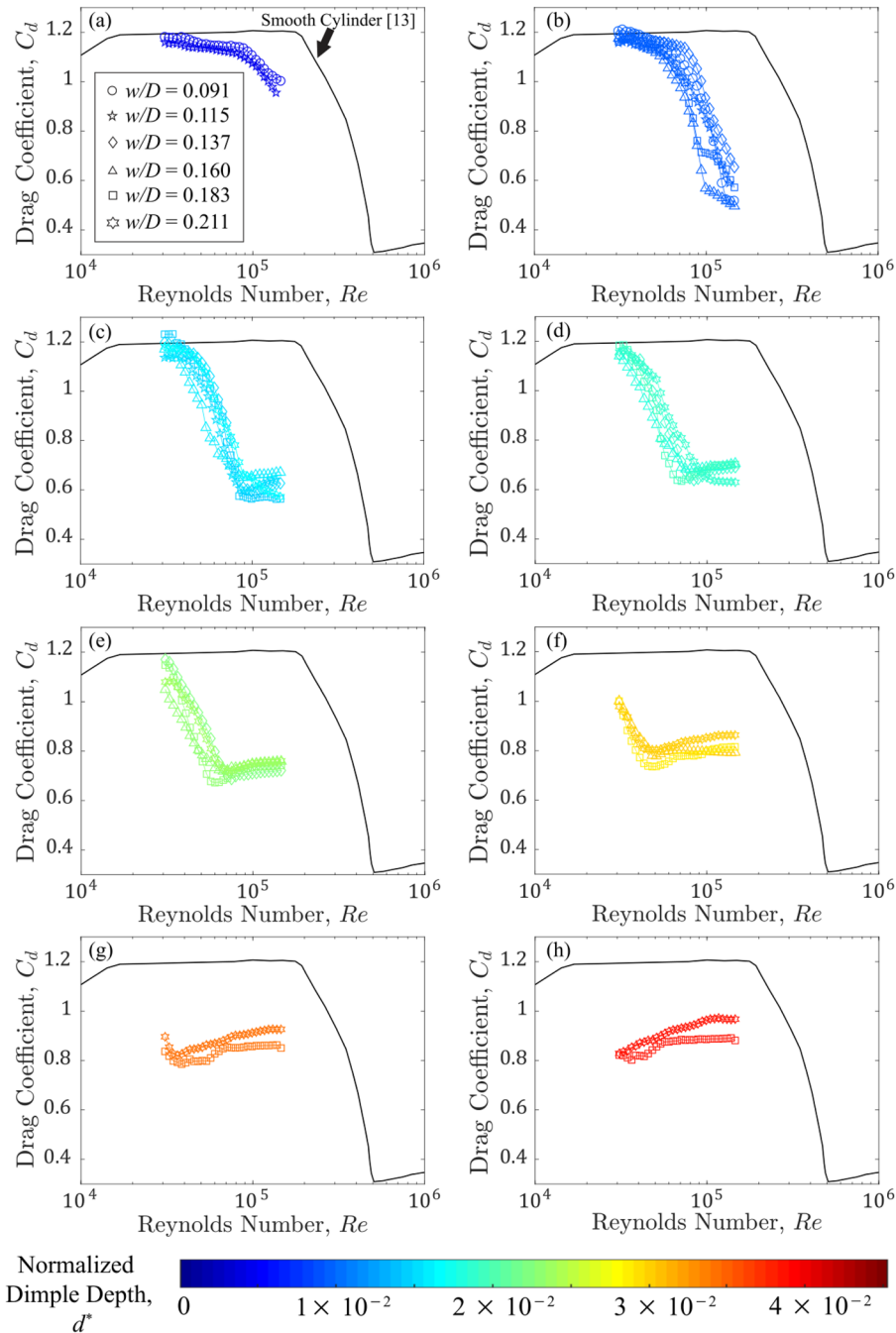


**Figure 5.** Effect of the normalized dimple depth on the dependence of the drag coefficient,  $C_d$ , on the Reynolds number,  $Re$ . Each panel shows results for wind tunnel experiments with different normalized dimple depths,  $d^*$ . For panels (a–h)  $d^* = \{0.5, 1.0, 1.6, 2.0, 2.4, 3.0, 3.4, \text{ and } 3.9 \pm 5\% \} \times 10^{-2}$ , respectively. The different symbols represent specimens with different dimple diameter to cylinder diameter ratios ( $0.091 \leq w/D \leq 0.211$ ). The black lines are the results of experiments by Wieselsberger<sup>[13]</sup> on a smooth cylinder.

$C_d = 0.9$  and 1.1. Figure 6b shows the results of active experiments in which we attempted to maintain a constant  $C_d = 0.9, 1.0$ , and 1.1 with the orange, magenta and yellow stars, respectively. For each of these active experiments, the same procedure was followed as described above for  $C_d = 1.0$ , and a fifth order polynomial was fit to the interpolated  $d^*$  versus  $Re$  data shown in Figure 6a.

Achieving a rapidly decreasing  $C_d$  (shown with the dark blue stars in Figure 6) was straightforward. Because of the presence of the critical regime in the drag crisis of a static specimen, we simply maintained a constant dimple depth, as shown by the dark blue line in Figure 6a. However, creating a system with a rapidly increasing  $C_d$ , could not be achieved with the same, constant  $d^*$  strategy. This is because, even after the critical

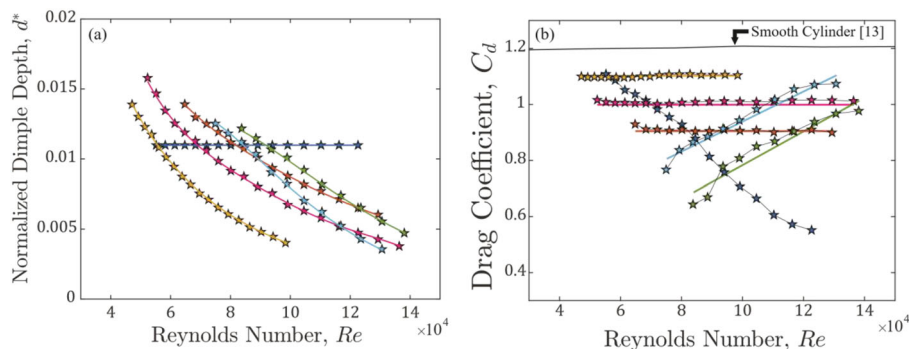


**Figure 6.** Programming of the drag coefficient profile. a) The normalized dimple depth,  $d^*$ , required to achieve the target  $C_d(Re)$  profile, for a specimen with  $w/D = 0.115$ . The solid lines are fits to a 5th order polynomial. b) Results for the experimentally obtained  $C_d(Re)$  profile (star symbols) versus the targeted profiles (solid lines). The black solid line corresponds to the results of experiments by Wieselsberger<sup>[13]</sup> on a smooth cylinder.

Reynolds number, the drag coefficient of dimpled specimens increases gradually. Following the methodology used to maintain a constant  $C_d$  – interpolating to find the required  $d^*$  and fitting a fifth order polynomial to the results – we were able to achieve a rapidly increasing  $C_d(Re)$ , as shown by the green and light blue stars in Figure 6.

Overall, we have demonstrated the possibility of programming a variety of  $C_d(Re)$  profiles that can be achieved by actively modifying the dimple depth as the wind speed changed. Nonetheless, the drag profiles that can be produced are not limited to the cases of a constant, rapidly increasing or rapidly decreasing  $C_d(Re)$ . Following the methodology of determining a continuous function,  $d^*(Re)$ , which achieves the desired  $C_d$ , other forms of  $C_d(Re)$  could be attained.

## 5. Conclusions

In summary, we have systematically investigated the aerodynamic performance of dimpled cylindrical samples with an active surface that can be pneumatically actuated. We experimentally studied the effect of the dimple depth and diameter on the dependence of the drag coefficient on the Reynolds number:  $C_d(Re)$ . Additionally, we used the tunable nature of the samples to program this dependence in a prescribed manner. A combination of mechanical experiments and FEM allowed us to characterize the topography of our morphable samples as a function of the pneumatic loading conditions. With these data (and a verified scaling law) at hand, we were then able to readily attain a target dimple profile by applying a set pressure differential. Through wind tunnel experiments, we first characterized the aerodynamic drag of our specimens, using fixed sample topographies, finding that the drag versus  $Re$  relationship depended solely on the dimple depth (not on the dimple diameter). We then developed an active control system in which we could automatically tune the surface shape as the flow conditions changed, in order to achieve a drag coefficient profile with a target functional dependency. While, as a proof-of-concept, we focused on a set of specific examples (linearly increasing/decreasing and constant  $C_d$  vs.  $Re$ ), the methodology we propose could be applied more broadly to a wide range of other desired drag profiles.

The ability to actively control the drag through manipulation of the surface shape could find applications in situations where bluff bodies are exposed to changing flow condition, for which structural resilience or fuel efficiency are important. We focused on the particular geometry of a cylinder to study this system. Additional studies should be performed on more complex geometries, including characterizing the dynamics of the flow structures produced downstream. Finally, while here we presented only one way to change the surface shape, future work could explore specimens with other activation mechanisms including particle-enhanced soft composites,<sup>[32]</sup> catalytic reactions,<sup>[33]</sup> or shape memory polymers.<sup>[34]</sup>

## Acknowledgement

This research was conducted with government support under and awarded by the Department of Defense (DoD) through the National Defense Science & Engineering Graduate Fellowship (NDSEG) Program, and by the National Science Foundation (CAREER Grant No. CMMI-1351449).

## Conflict of Interest

The authors declare no conflict of interest.

## Keywords

aerodynamic drag, drag reduction, morphable surfaces, programmable function, smart structures

Received: December 11, 2018

Revised: March 1, 2019

Published online:

- [1] P. Bearman, J. Harvey, *Aeronaut. Q.* **1976**, *27*, 112.
- [2] W. Taylor, Golf ball. *US Patent 878254*, **1908**.
- [3] H. Choi, W.-P. Jeon, J. Kim, *Annu. Rev. Fluid Mech.* **2008**, *40*, 113.
- [4] J. Choi, *Ph. D. Thesis*, Seoul Natl. Univ., Korea, **2006**.
- [5] J. Choi, W. P. Jeon, H. Choi, *Phys. Fluids* **2006**, *18*, 041702.

- [6] P. Bearman, J. Harvey, *AIAA J.* **1993**, *31*, 1753.  
 [7] J. M. Davies, *J. Appl. Phys.* **1949**, *20*, 821.  
 [8] R. D. Mehta, *Annu. Rev. Fluid Mech.* **1985**, *17*, 151.  
 [9] F. Alam, T. Steiner, H. Chowdhury, H. Moria, I. Khan, F. Aldawi, A. Subic, *Procedia Eng.* **2011**, *13*, 226.  
 [10] A. Norman, E. Kerrigan, B. McKeon, *J. Fluid Mech.* **2011**, *675*, 268.  
 [11] A. Norman, B. McKeon, *Exp. Fluids* **2011**, *51*, 1031.  
 [12] S. Raayai-Ardakani, G. H. McKinley, *Phys. Fluids* **2017**, *29*, 093605.  
 [13] C. Wieselsberger, *Phys. Z.* **1921**, *22*, 321–328.  
 [14] A. Roshko, *J. Fluid Mech.* **1961**, *10*, 345.  
 [15] E. Achenbach, *J. Fluid Mech.* **1972**, *54*, 565.  
 [16] E. Achenbach, *J. Fluid Mech.* **1974**, *65*, 113.  
 [17] K. Aoki, K. Muto, H. Okanaga, *J. Fluid Sci. Technol.* **2012**, *7*, 1.  
 [18] D. Terwagne, M. Brojan, P. M. Reis, *Adv. Mater.* **2014**, *26*, 6659.  
 [19] E. Achenbach, *J. Fluid Mech.* **1971**, *46*, 321.  
 [20] U. Butt, C. Egbers, *Int. J. Mater. Mech. Manuf.* **2013**, *1*, 121.  
 [21] B. Zhou, X. Wang, W. Guo, W. M. Ghossein, S. K. Tan, *Exp. Therm. Fluid Sci.* **2015**, *69*, 19.  
 [22] M. Gutttag, P. M. Reis, *Phys. Rev. Fluids* **2017**, *2*, 123903.  
 [23] P. T. Tokumaru, P. E. Dimotakis, *J. Fluid Mech.* **1991**, *224*, 77.  
 [24] D. Shiels, A. Leonard, *J. Fluid Mech.* **2001**, *431*, 297.  
 [25] J.-W. He, R. Glowinski, R. Metcalfe, A. Nordlander, J. Periaux, *J. Comput. Phys.* **2000**, *163*, 83.  
 [26] R. D. Blevins, *Flow-Induced Vibration*, 2nd ed., Van Nostrand Reinhold Co., Inc., New York, NY **1990**.  
 [27] R. E. D. Bishop, A. Y. Hassan, *Proc. R. Soc. A* **1964**, *277*, 51.  
 [28] S. Jeon, J. Choi, W.-P. Jeon, H. Choi, J. Park, *J. Fluid Mech.* **2004**, *517*, 113.  
 [29] J. Kim, H. Choi, *Phys. Fluids* **2005**, *17*, 033103.  
 [30] Z. Cao, P. Wang, W. Gao, L. Tao, J. W. Suk, R. S. Ruoff, D. Akinwande, R. Huang, K. M. Liechti, *Carbon* **2014**, *69*, 390.  
 [31] E. Maskell, *Aeronautical Research Council (Great Britain)*, R&M Report No. 3400 **1965**.  
 [32] M. Gutttag, M. Boyce, *Adv. Funct. Mater.* **2015**, *25*, 3641.  
 [33] M. Wehner, R. L. Truby, D. J. Fitzgerald, B. Mosadegh, G. M. Whitesides, J. A. Lewis, R. J. Wood, *Nature* **2016**, *536*, 451.  
 [34] H. Meng, G. Li, *Polymer* **2013**, *54*, 2199.